Anode-supported intermediate temperature direct internal reforming solid oxide fuel cell. I: model-based steady-state performance

P. Aguiar[a], C.S. Adjiman[a,b], N.P. Brandon[a,*]

[a] *Department of Chemical Engineering and Chemical Technology, Imperial College London, London SW7 2AZ, UK*
[b] *Centre for Process Systems Engineering, Imperial College London, London SW7 2AZ, UK*

Abstract

Mathematical modelling is an essential tool for the design of solid oxide fuel cells (SOFCs). The present paper aims to report on the development of a dynamic anode-supported intermediate temperature direct internal reforming planar solid oxide fuel cell stack model, that allows for both co-flow and counter-flow operation. The developed model consists of mass and energy balances, and an electrochemical model that relates the fuel and air gas composition and temperature to voltage, current density, and other relevant fuel cell variables. The electrochemical performance of the cell is analysed for several temperatures and fuel utilisations, by means of the voltage and power density versus current density curves. The steady-state performance of the cell and the impact of changes in fuel and air inlet temperatures, fuel utilisation, average current density, and flow configuration are studied. For a co-flow SOFC operating on a 10% pre-reformed methane fuel mixture with 75% fuel utilisation, inlet fuel and air temperatures of 1023 K, average current density of 0.5 A cm^{-2}, and an air ratio of 8.5, an output voltage of 0.66 V with a power density of 0.33 W cm^{-2} and a fuel efficiency of 47%, are predicted. It was found that cathode activation overpotentials represent the major source of voltage loss, followed by anode activation overpotentials and ohmic losses. For the same operating conditions, SOFC operation under counter-flow of the fuel and air gas streams has been shown to lead to steep temperature gradients and uneven current density distributions.
© 2004 Elsevier B.V. All rights reserved.

Keywords: Anode-supported; Intermediate temperature; Direct internal reforming; SOFC; Planar; Dynamic model

1. Introduction

Solid oxide fuel cells (SOFCs) are energy conversion devices that produce electricity and heat directly from a gaseous or gasified fuel by electrochemical combination of that fuel with an oxidant. A SOFC consists of an interconnect structure and a three-layer region composed of two ceramic electrodes, anode and cathode, separated by a dense ceramic electrolyte (often referred to as the PEN—Positive-electrode/Electrolyte/Negative-electrode). SOFCs operate at high temperatures and atmospheric or elevated pressures, and can use hydrogen, carbon monoxide, and hydrocarbons as fuel, and air (or oxygen) as oxidant. In the cell, the oxygen ions formed at the cathode migrate through the ion-conducting electrolyte to the anode/electrolyte interface where they react with the hydrogen and carbon monoxide contained in (and/or produced by) the fuel, producing water and carbon dioxide while releasing electrons that flow via an external circuit to the cathode/electrolyte interface [1]. An oxygen chemical potential gradient is formed across the electrolyte by burning fuel with oxygen on the anode, while leaving the cathode exposed to abundant atmospheric oxygen.

While conventional high-temperature SOFCs generally operate between 1073 and 1273 K, a number of research groups are presently focusing on intermediate temperature-solid oxide fuel cells (IT-SOFCs). These typically operate

---

* Corresponding author. Tel.: +44 20 7594 5704; fax: +44 20 7594 5604.
  E-mail address: n.brandon@imperial.ac.uk (N.P. Brandon).

Nomenclature

ASR	area specific resistance ($\Omega\,m^2$)
c_p	specific heat capacity of the gas streams, PEN structure, and interconnect ($kJ\,kg^{-1}\,K^{-1}$)
C_i	molar concentration of component i ($mol\,m^{-3}$)
d_h	hydraulic diameter of a rectangular cross-section gas channel (m)
$D_{bulk,i}$	bulk diffusivity coefficient ($m^2\,s^{-1}$)
$D_{eff,electrode}$	electrode effective diffusivity coefficient ($m^2\,s^{-1}$)
$D_{Knudsen,i}$	Knudsen diffusivity coefficient ($m^2\,s^{-1}$)
$D_{molecular,i}$	molecular diffusivity coefficient for component i ($m^2\,s^{-1}$)
D_x	axial diffusion coefficient ($m^2\,s^{-1}$)
E_a	activation energy ($kJ\,mol^{-1}$)
$E_{electrode}$	activation energy of the exchange current density ($kJ\,mol^{-1}$)
F	Faraday's constant ($C\,mol^{-1}$)
F_{air}	molar flow rate of the air stream ($mol\,s^{-1}$)
F_{fuel}	molar flow rate of the fuel stream ($mol\,s^{-1}$)
h_a	air channel height (m)
h_f	fuel channel height (m)
$\bar{j}$, j	average and local current density ($A\,m^{-2}$)
$j_{0,electrode}$	exchange current density ($A\,m^{-2}$)
$k_{a,I}$, $k_{a,PEN}$	air channel heat transfer coefficient ($kJ\,m^{-2}\,s^{-1}\,K^{-1}$) (Table 4)
$k_{electrode}$	pre-exponential factor of the exchange current density ($A\,m^{-2}$)
$k_{f,I}$, $k_{f,PEN}$	fuel channel heat transfer coefficient ($kJ\,m^{-2}\,s^{-1}\,K^{-1}$) (Table 4)
k_H	equilibrium constant for hydrogen adsorption (Table 3)
k_S	equilibrium constant for steam adsorption (Table 3)
k_0	pre-exponential constant (Table 3)
L	system length (m)
LHV	lower heating value
n	number of electrons participating in the electrochemical reaction
Nu	Nusselt number
P	pressure (bar)
Pe	Peclet number $Pe = uL/D_x$
p_i	partial pressure of component i in relevant gas channel (bar)
$p_{i,TPB}$	partial pressure of component i at relevant three phase boundary (bar)
P_{SOFC}	power density ($W\,m^{-2}$)
R_k	rate of reaction k ($mol\,m^{-2}\,s^{-1}$)
R_{Ohm}	total cell resistance, including both ionic and electronic resistances ($\Omega\,m^2$)
$\Re$	gas constant ($kJ\,mol^{-1}\,K^{-1}$)
t	time (s)
T	temperature (K)
u_a	air velocity ($m\,s^{-1}$)
u_f	fuel velocity ($m\,s^{-1}$)
U	potential (V)
U^{OCP}	open-circuit potential (OCP) (V)
$U_{H_2}^0$	OCP for standard temperature and pressure and pure reactants for the H_2 oxidation reaction (V)
U_{fuel}	fuel utilisation factor
W	system width (m)
x	axial coordinate (m)
y_i	molar fraction of component i
y_i^0	molar fraction of component i at inlet

Greek letters

α	transfer coefficient
β_1, β_2	methane and steam order of reaction (Table 3)
β_3	number of surface sites required for methane adsorption (Table 3)
$(-\Delta H)_k$	enthalpy change of reaction k ($kJ\,mol^{-1}$)
$\in$	emissivity
λ_{air}	air ratio
λ_a, λ_f, λ_{PEN}, λ_I	thermal conductivity of the gas streams, PEN structure, and interconnect ($kJ\,m^{-1}\,s^{-1}\,K^{-1}$)
ε_p	electrode porosity
ε_{SOFC}	fuel cell efficiency
η_{act}	activation overpotential losses (V)
η_{conc}	total concentration overpotential losses (V)
$\eta_{conc,electrode}$	concentration overpotential losses (V)
σ	Stefan–Boltzmann constant ($W\,m^{-2}\,K^{-4}$)
σ_{anode}, $\sigma_{cathode}$	electronic conductivity of the anode and cathode ($\Omega^{-1}\,m^{-1}$)
$\sigma_{electrolyte}$	ionic conductivity of the electrolyte ($\Omega^{-1}\,m^{-1}$)
ρ_a, ρ_f, ρ_{PEN}, ρ_I	density of the gas streams, PEN structure, and interconnect ($kg\,m^{-3}$)
τ_{anode}, $\tau_{cathode}$	thickness (m)
$\tau_{electrolyte}$, τ_{PEN}, τ_I, $\tau_{tortuosity}$	tortuosity
v_{ik}	stoichiometric coefficient of component i in reaction k

Superscripts

0	feed conditions (fuel and air channel inlet)

Subscripts

a	air channel
act	activation
conc	concentration
f	fuel channel
i	component
I	interconnect
k	reaction
Ohm	Ohmic
PEN	PEN structure
TPB	three-phase boundary

between 823 and 1073 K, allowing for a wider range of materials and more cost-effective SOFC fabrication, particularly in relation to the interconnections and balance of plant (BoP). High-temperature SOFCs are generally all ceramic while intermediate temperature SOFCs are metal-ceramic and use stainless steel interconnects instead of more expensive high-chrome alloys or oxides. A typical SOFC electrolyte is yttria-stabilised zirconia (YSZ), an oxide ion conductor at elevated temperatures. The anode is usually a nickel/zirconia cermet, which provides high electrochemical performance, good chemical stability, and low cost, and the cathode a perovskite material, such as strontium doped lanthanum manganite, often mixed with YSZ in the form of a composite [2,3]. Two main SOFC designs are the electrolyte-supported and electrode-supported SOFC. In the former design, the electrolyte is the thickest component and works as the support structure. Electrolyte-supported cells are only suitable for high-temperature operation where the, often large, ohmic losses can be reduced. Electrode-supported SOFCs have been developed in an attempt to minimise such ohmic losses under lower temperature operation, as in the case of IT-SOFCs. In these cells, one of the two electrodes is the thickest component and support structure, while the electrolyte is required to have high ionic conductivity and/or small thickness. However, it is usually observed that, despite a low ohmic contribution, the area specific resistance of IT-SOFCs may be larger than high-temperature SOFCs. This is due to activation, and perhaps concentration overpotentials, that can often outweigh the ohmic contribution. Thus, many of the recent efforts in fuel cell technology development have been devoted to reducing the thickness of critical cell components while refining and improving the electrode structure and electrolyte phase, with the aim of obtaining a higher and more stable electrochemical performance, while lowering cost [4–6].

Most fuel cells need to convert a hydrocarbon primary fuel into a hydrogen-rich gas required for the electrochemical reaction on the anode side. One option for converting the hydrocarbon feed is to do it indirectly in a fuel processing system, such as an external catalytic steam reformer or partial oxidation reactor [7,8]. In the most common case of a reformer, heat needs to be available to drive the steam reforming reaction. One method of achieving this is to feed the exhaust gases from the anode and cathode into a burner where the excess fuel is combusted. The heat generated in the burner can then be used to preheat both the steam and the fuel, and provide the heat needed in the reformer. However, a more elegant and efficient method of providing heat for reforming in fuel cell systems is to carry out the reforming in the cell stack [9,10]. Catalytic steam reforming of hydrocarbons is typically performed between 1023 and 1173 K, and is thus compatible with SOFCs. These operate at high enough temperatures for the endothermic steam reforming reaction to be carried out within the stack, giving rise to an internal reforming SOFC (IR-SOFC). Depending on the operating conditions, the heat for the reforming reaction can vary from 40 to 70% of the total heat produced in a fuel cell. Thus, internal reforming fuel cells eliminate the requirement for a separate fuel reformer, leading to a more attractive and efficient system design; the requirement for cell cooling, which is usually achieved by flowing excess air through the cathode, is also significantly reduced [11,12]. There are two main approaches to internal reforming within a fuel cell: indirect or integrated (IIR) and direct (DIR) internal reforming. In the first approach, the reformer section is separate but adjacent to the fuel cell anode and in close thermal contact with it. In the latter approach, methane is fed directly into the cell and the reforming takes place directly on the anode [9]. One advantage of IIR is that the reformer and cell environments do not have a direct physical effect on each other; however, the conversion of methane to hydrogen is not promoted to the same extent as with direct internal reforming. For a DIR configuration, part of the steam required for the reforming reaction can be obtained from the fuel cell electrochemical oxidation of hydrogen and, because of the continuing consumption of hydrogen, the equilibrium of the reforming reaction may be further shifted to the right, increasing the methane conversion [13] and leading to a more evenly distributed load of hydrogen. However, the DIR approach requires an anode material that possesses good catalytic properties for steam reforming as well as for effective generation of power [12]. In a SOFC, the reforming may occur internally: it has been shown that the state-of-the-art SOFC nickel/zirconia cermet anodes can provide sufficient activity for the steam reforming and shift reactions without the need for any additional catalyst [7,9]. A problem related to DIR is carbon deposition on the anode and subsequent electrocatalyst deactivation, leading to loss of cell performance and poor durability. The high steam/carbon ratio typically used in conventional steam reformers to suppress carbon formation is unattractive as it lowers the electrical efficiency of the fuel cell by steam dilution of the fuel [14]. Hence, advanced anode materials that allow for direct internal reforming at low steam/carbon ratios could offer significant benefits. A second problem, mostly related to high-temperature SOFCs, is the strong cooling effect caused by the highly endothermic reforming reaction that can generate large temperature gradients across the cell and limit the amount of internal reforming allowed in practice. It has been shown that in high-temperature IR-SOFCs, all the methane is usually completely reformed within a small distance from the anode entrance [15–18]. IT-SOFCs also offer significant advantages in terms of internally reforming methane, as the lower temperature naturally reduces the reforming reaction rate, without the need for any catalyst modification or complex cell design.

Mathematical modelling is an essential tool in the design of fuel cell systems, as it is important to understand the response of a cell stack under normal or transient conditions. Such models can provide a picture of cell stress, potential, current density, and temperature as functions of position and time, for various cell configurations and operating conditions, and be used to examine the effects of changes on one or

more variables and the relative system sensitivity to relevant design parameters. A model is also useful in predicting the effects of altering process variables and in using that information to optimise cell performance. The main aims of this paper are to: present a dynamic model of a planar anode-supported intermediate temperature SOFC stack with direct internal reforming; investigate the steady-state performance of such SOFC system; and analyse the impact of changes in inlet temperature, fuel utilisation, average current density, and flow configuration. Although, the full dynamic SOFC model has been developed and is explained here, the present paper only explores the cell steady-state performance. A subsequent publication will deal with its dynamic aspects [19].

2. SOFC mathematical model

There have been several publications focusing on modelling the performance of high-temperature SOFCs. Such models can be for different geometries (tubular, planar, or monolithic), PEN structures (electrolyte or electrode-supported), and flow configurations (cross-, co-, or counter-flow); can range from one to three-dimensional; and can consider or ignore internal reforming or various other phenomena [1,15,20–25]. Even though most of the work found is for SOFC steady-state performance, dynamic issues have also been addressed by some authors [26–29]. The dynamic intermediate temperature SOFC model developed here is one-dimensional and allows for co- and counter-flow operation, although the equations presented next are for the co-flow case only.

To produce a useful voltage, a complete SOFC system can not be made up of a single solid oxide fuel cell, as its voltage is quite small (about 0.7 V when drawing a useful current), but must consist of several repeating electrochemical cells in a module, connected both in series and/or in parallel and assembled to compose a stack. However, models of SOFCs are usually developed for the smallest unit cell or module. Such models can then be used to compute the operating conditions of the whole stack provided that the boundary conditions for each unit cell are independent and that adequate boundary conditions are established for the stack exterior. In the case reported here, the repeating single-cell is considered to be in the centre of a large stack, such that no end effects are present, and to be formed when two interconnect plates are placed above and below an electrochemically active tri-layer cell composed of the anode, electrolyte, and cathode (PEN structure). Interconnect plates normally provide the internal gas flow manifolds and flow passages above and below the PEN; the individual gas flow channels are neglected in the present model. Fig. 1 shows a schematic view of a vertical slice through a *y–z* plane of a multiple-cell, planar, co-flow stack, where the fuel and air gas streams flow along the *x*-direction. For the purpose of modelling, it is considered that the SOFC is composed of the fuel and air channels, the PEN structure, and the interconnect. The model developed con-
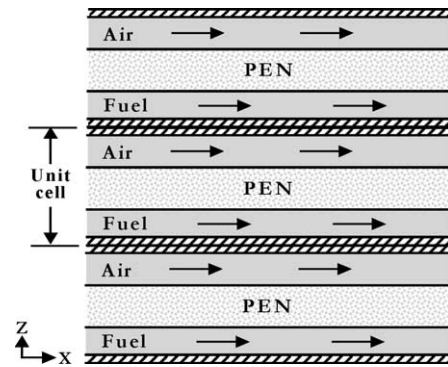

Fig. 1. Schematic side view of a co-flow planar SOFC stack.

sists of: two mass balances, to the fuel and air channels; four energy balances, to the fuel and air channels, PEN, and interconnect; and an electrochemical model that relates the fuel and air gas composition and temperature to the voltage, current density, and other cell variables. Pressure drop along the channels is neglected. Note that for the development of such a model, several simplifying assumptions (namely, the variation of some gas/solid properties along the fuel cell length and with time) were made to obtain a more computationally tractable dynamic model. Although it is believed that any differences between the results predicted with this model or with a more refined one will not be significant, such a model will also be developed in the near future and the results obtained reported.

2.1. Mass balances

For the mass balance in the fuel channel, the chemical species considered are CH_4, H_2O, CO, H_2, and CO_2, while for the air channel the chemical species are O_2 and N_2 (as the oxidant is considered to be air and not pure oxygen). The molar flux in these gas channels is considered convective in the flow direction. Given the high aspect ratio and Peclet number values, *Pe*, it was found reasonable to neglect axial dispersion effects. Table 1 presents the fuel and air channel mass balances. In SOFCs, the presence of CO and CO_2 in the fuel does not poison the anode reaction, and indeed CO can function as a fuel. Nevertheless, here it is assumed that only hydrogen is electrochemically oxidised and that all the CO is converted through the shift reaction, considered to be at equilibrium [30–32]. It is also assumed that any methane present in the fuel channel can only be reformed to H_2, CO, and CO_2 and, hence, not electrochemically oxidised. Thus, in the fuel channel, three reactions are taken into account: methane steam reforming (i), water gas-shift (ii), and hydrogen electrochemical oxidation (iii). In the air channel, only the reduction reaction of O_2 to O^{2-} ions is considered (iv). Table 2 presents all these reactions. It should be noted that $R_{(iii)} = R_{(iv)} = R_{(v)}$ where $R_{(v)}$ stands for the hydrogen oxidation reaction rate. Faraday's law relates the flux of reactants and products to the electric current arising from an electro-

chemical reaction. According to this law, and when only H_2 oxidation is present, the local amount of H_2 and O_2 consumed and H_2O produced through reaction (v) in Table 2 is related to the local electric current density, j, produced in the cell by

$$R_{(v)} = \frac{j}{2F}. \tag{1}$$

This relation relies on the fact that solid electrolytes such as YSZ are pure ionic conductors, and so only oxygen ions can permeate through the electrolyte to take part in the oxidation reaction at the anode/electrolyte interface [33].

As for the kinetics of the reforming reaction, although conventional methane steam reforming has been widely studied and there are several publications dealing with its kinetics and catalytic aspects [34–36], there is only a small amount of data available for the kinetics of reforming in SOFC anodes. Table 3 presents some of the rate equations published so far for Ni cermet anodes.

Lee et al. [12] studied methane conversion with different Ni/ZrO$_2$ anode materials. For 60 vol.% Ni cermets, they found an activation energy of 98 kJ mol^{-1}. Achenbach and Riensche [18] and Belyaev et al. [37] both showed that the steam reforming reaction rate was first order in methane and zero order in water, for a 80 wt.% ZrO$_2$ and 20 wt.% Ni cermet and for a mixed Ni-(5 wt.%) ZrO$_2$-(2 wt.%) CeO$_2$ anode, respectively. Dicks et al. [38] studied the methane reforming rate given by a thin electrolyte-supported Ni–YSZ anode using a tubular plug flow differential reactor. Ahmed and Foger [13] investigated Ni–YSZ and Ni–YSZ modified (addition of a basic compound) anodes. They found that the reaction order in CH$_4$ increased from 0.85 for the

Table 1
Dynamic SOFC model: mass balances

Fuel channel

$$\frac{\partial C_{i,f}}{\partial t} = -u_f \frac{\partial C_{i,f}}{\partial x} + \sum_{k \in \{(i),(ii),(v)\}} v_{i,k} R_k \frac{1}{h_f}$$

$$i \in \{CH_4, H_2O, CO, H_2, CO_2\} \tag{2}$$

$$C_{i,f}|_{x=0} = C_i^0 \quad i \in \{CH_4, H_2O, CO, H_2, CO_2\} \tag{3}$$

Air channel

$$\frac{\partial C_{i,a}}{\partial t} = -u_a \frac{\partial C_{i,a}}{\partial x} + v_{i,(v)} R_{(v)} \frac{1}{h_a} \quad i \in \{O_2, N_2\} \tag{4}$$

$$C_{i,a}|_{x=0} = C_i^0 \quad i \in \{O_2, N_2\} \tag{5}$$

Table 2
Reactions considered in the mass and energy balances

Steam reforming reaction	(i) $CH_4 + H_2O \Leftrightarrow CO + 3H_2$
Water gas-shift reaction	(ii) $CO + H_2O \Leftrightarrow CO_2 + H_2$
Hydrogen oxidation reaction	(iii) $H_2 + O^{2-} \rightarrow H_2O + 2e^-$
Oxygen reduction reaction	(iv) $\frac{1}{2}O_2 + 2e^- \rightarrow O^{2-}$
Overall cell reaction	(v) $H_2 + \frac{1}{2}O_2 \rightarrow H_2O$

Table 3
Rate equations for methane reforming on nickel cermet SOFC anodes

Kinetic equation		Reference
$R_{(i)} = k_0 p_{CH_4} p_{H_2O}^{-1.25} \exp\left(-\frac{E_a}{\Re T}\right)$	(6)	[12]
(7) $R_{(i)} = k_0 p_{CH_4} \exp\left(-\frac{E_a}{\Re T}\right)$	(7)	[18,37]
$R_{(i)} = k_0 p_{CH_4} \left(1 + k_H p_{H_2}^{0.5} + k_S \frac{p_{H_2O}}{p_{H_2}}\right)^{-\beta_3} \exp\left(-\frac{E_a}{\Re T}\right)$ (8)		[38]
(9) $R_{(i)} = k_0 p_{CH_4}^{\beta_1} p_{H_2O}^{\beta_2} \exp\left(-\frac{E_a}{\Re T}\right)$	(9)	[13]

Ni–YSZ anode to 1.4 for the modified anode, the order in steam changed from −0.35 to −0.8, and the activation energy from 95 to 210 kJ mol^{-1}. Other kinetic expressions and a review in advances of DIR catalysts can be found in references [7,9,11,32,39,40]. For the fuel channel mass and energy balances, the first order kinetic expression derived by Achenbach and Riensche [18] and presented in Table 3, with an activation energy of $E_a = 82$ kJ mol^{-1} and a pre-exponential constant of $k_0 = 4274$ mol s^{-1} m^{-2} bar^{-1}, has been adopted. Such a kinetic expression is considered typical of DIR-SOFC performance.

As mentioned previously, the water gas-shift reaction (ii) is considered to be at equilibrium in the fuel channel; an equilibrium-limited shift reaction rate expression, first order in carbon monoxide and with an arbitrarily high pre-exponential factor k_{WGSR}, given by

$$R_{(ii)} = k_{WGSR} p_{CO} \left(1 - \frac{p_{CO_2} p_{H_2}/p_{CO} p_{H_2O}}{K_{eq,(ii)}}\right), \tag{10}$$

is used to consider this effect.

2.2. Energy balances

In a fuel cell, current and temperature distributions are strongly coupled. Therefore, knowledge of the prime heat transfer processes is required. Such processes include heat release arising from electrochemical reactions, electrical resistances, and/or anode fuel chemistry; convective heat transfer between cell components and fuel and air gas streams; and in-plane heat conduction through cell components. Many authors have made different assumptions when modelling heat transfer within a SOFC. The model in Table 4 considers that the thermal flux in the PEN and interconnect structures is conductive and modelled by Fourier's law of heat conduction, and in the gas channels is convective in the gas flow direction and from the gas channels to the solid parts [1,24]. The heat transfer coefficients between the gas channels and the solid parts were calculated using a constant Nusselt number, Nu (a common assumption given the laminar flow conditions for

which the Nusselt number is considered independent of the Reynolds number) and the channel hydraulic diameter [41]. Thus, $k_{f,PEN}$, $k_{f,I}$, $k_{a,PEN}$, and $k_{a,I}$ are given by:

$$k_{f,PEN} = k_{f,I} = Nu \frac{\lambda_f}{d_{h,f}}, \quad d_{h,f} = \frac{2Wh_f}{W + h_f} \quad (11)$$

$$k_{a,PEN} = k_{a,I} = Nu \frac{\lambda_a}{d_{h,a}}, \quad d_{h,a} = \frac{2Wh_a}{W + h_a} \quad (12)$$

Table 4
Dynamic SOFC model: energy balances

Fuel channel

$$\rho_f c_{p,f} \frac{\partial T_f}{\partial t} = -u_f \rho_f c_{p,f} \frac{\partial T_f}{\partial x} + k_{f,PEN}(T_{PEN} - T_f)\frac{1}{h_f} + k_{f,I}(T_I - T_f)\frac{1}{h_f}$$
$$+ \sum_{k \in \{(i),(ii)\}} (-\Delta H)_k R_k \frac{1}{h_f} \quad (13)$$

$$T_f|_{x=0} = T_f^0 \quad (14)$$

Air channel

$$\rho_a c_{p,a} \frac{\partial T_a}{\partial t} = -u_a \rho_a c_{p,a} \frac{\partial T_a}{\partial x} + k_{a,PEN}(T_{PEN} - T_a)\frac{1}{h_a}$$
$$+ k_{a,I}(T_I - T_a)\frac{1}{h_a} \quad (15)$$

$$T_a|_{x=0} = T_a^0 \quad (16)$$

PEN structure

$$\rho_{PEN} c_{p,PEN} \frac{\partial T_{PEN}}{\partial t} = \lambda_{PEN} \frac{\partial^2 T_{PEN}}{\partial x^2} - k_{f,PEN}(T_{PEN} - T_f)\frac{1}{\tau_{PEN}}$$
$$- k_{a,PEN}(T_{PEN} - T_a)\frac{1}{\tau_{PEN}}$$
$$+ [(-\Delta H)_{(v)} R_{(v)} - jU]\frac{1}{\tau_{PEN}}$$
$$+ \left[\frac{\sigma(T_I^4 - T_{PEN}^4)}{1/\epsilon_I + 1/\epsilon_{PEN} - 1} \right] \frac{1}{\tau_{PEN}} \quad (17)$$

$$\text{where} \quad \tau_{PEN} = \tau_{anode} + \tau_{electrolyte} + \tau_{cathode} \quad (18)$$

$$\left. \frac{\partial T_{PEN}}{\partial x} \right|_{x=0} = 0, \quad \left. \frac{\partial T_{PEN}}{\partial x} \right|_{x=L} = 0 \quad (19)$$

Interconnect

$$\rho_I c_{p,I} \frac{\partial T_I}{\partial t} = \lambda_I \frac{\partial^2 T_I}{\partial x^2} - k_{f,I}(T_I - T_f)\frac{1}{\tau_I} - k_{a,I}(T_I - T_a)\frac{1}{\tau_I}$$
$$- \left[\frac{\sigma(T_I^4 - T_{PEN}^4)}{1/\epsilon_I + 1/\epsilon_{PEN} - 1} \right] \frac{1}{\tau_I} \quad (20)$$

$$\left. \frac{\partial T_I}{\partial x} \right|_{x=0} = 0, \quad \left. \frac{\partial T_I}{\partial x} \right|_{x=L} = 0 \quad (21)$$

where λ_f (λ_a) denotes the thermal conductivity of the fuel (air) stream and $d_{h,f}$ ($d_{h,a}$) the hydraulic diameter of the fuel (air) channel. Here, the Nusselt number is taken to be 3.09 [42]. Due to the high temperatures involved, radiation between the PEN structure and interconnect is also included. For this purpose, the general expression for heat transfer by radiation between two infinite parallel planes is considered [43]. It is assumed that the hydrogen oxidation reaction enthalpy is released at the PEN structure [29] and that, as the cell being modelled is placed in the central region of a stack, there is no heat flux through the external walls [22]. Finally, it is also assumed that the overall effect of the variation of the gas densities, heat capacities and velocities can be neglected.

2.3. Electrochemical model

The difference between the thermodynamic potentials of the electrode reactions determines the reversible cell voltage or open-circuit potential, U^{OCP} [44,45]. This open-circuit potential is a local quantity, as it depends on the gas composition and temperature at the electrodes, and can be determined by the Nernst Eq. (22) written for the electrochemical oxidation of hydrogen. $U_{H_2}^0$ stands for the open-circuit potential at standard temperature and pressure and unity activity, and is a function of the Gibbs free energy change for the H_2 oxidation reaction.

$$U^{OCP} = U_{H_2}^0 - \frac{\Re T}{2F} \ln \left(\frac{p_{H_2O,f}}{p_{H_2,f} p_{O_2,a}^{1/2}} \right) \quad (22)$$

The theoretical open-circuit voltage is the maximum voltage that can be achieved by a fuel cell under specific operating conditions. However, the voltage of an operating cell, U, equal to the voltage difference between the cathode and the anode, is generally lower than this. As current is drawn from a fuel cell, the cell voltage falls due to internal resistances and overpotential losses. Electrode overpotential losses are associated with the electrochemical reactions taking place at the electrode/electrolyte interfaces and can be divided into concentration and activation overpotentials. These losses are common to all types of fuel cells and cannot be eliminated, although temperature, pressure, gas flow rate and composition, electrode and electrolyte materials, and cell design, all influence their magnitude. The voltage or potential of an operating cell is thus generically given by Eq. (23), that can be derived from Kirchoff's and Ohm's laws by considering a cell as many small elements in series, and each one of those elements as a local battery with its own internal resistance.

$$U = U^{OCP} - (\eta_{Ohm} + \eta_{conc,anode} + \eta_{conc,cathode} + \eta_{act,anode}$$
$$+ \eta_{act,cathode}). \quad (23)$$

η_{Ohm} stands for the ohmic losses and $\eta_{conc,anode}$, $\eta_{conc,cathode}$, $\eta_{act,anode}$, and $\eta_{act,cathode}$ for the anode and cathode concentration and activation overpotential losses. All these losses are in part responsible for the heat produced in an operating

fuel cell and are explained next. As both electrodes are normally good conductors, a constant cell voltage throughout the cell is normally considered [46].

2.3.1. Ohmic losses

Ohmic losses are caused by resistance to conduction of ions (through the electrolyte) and electrons (through the electrodes and current collectors) and by contact resistance between cell components. This voltage drop is important in all types of cells and is essentially linear and proportional to current density. Because the ionic flow in the electrolyte and the electronic flow in the electrodes obey Ohm's law, ohmic losses can be expressed by

$$\eta_{\text{Ohm}} = j R_{\text{Ohm}}, \tag{24}$$

where j is the current density and R_{Ohm} the internal resistance of the cell, which includes electronic and ionic resistances. R_{Ohm} can be obtained from measured cell resistances or be estimated from the effective distance between the components coupled with conductivity data. Here, R_{Ohm} is calculated from the conductivity of the individual layers (assuming negligible contact resistances, cross-plane charge flow, and series connection of resistances) by:

$$R_{\text{Ohm}} = \frac{\tau_{\text{anode}}}{\sigma_{\text{anode}}} + \frac{\tau_{\text{electrolyte}}}{\sigma_{\text{electrolyte}}} + \frac{\tau_{\text{cathode}}}{\sigma_{\text{cathode}}}, \tag{25}$$

where τ_{anode}, $\tau_{\text{electrolyte}}$, and τ_{cathode} stand for the thickness of the anode, electrolyte, and cathode layers, σ_{anode} and σ_{cathode} for the electronic conductivity of the anode and cathode, and $\sigma_{\text{electrolyte}}$ for the ionic conductivity of the electrolyte [47].

2.3.2. Concentration overpotentials

Concentration overpotentials appear when mass transport effects hinder the electrode reaction, i.e. when the reactant inlet flux and the product outlet flux from an electrode are slower than that corresponding to the discharged current, and concentration profiles develop across the electrodes. Physical processes that contribute to the occurrence of concentration overpotentials include gas species molecular transport in the electrode pores, solution of reactants into the electrolyte, dissolution of products out of the electrolyte, and diffusion of the reactants/products through the electrolyte to/from the reaction sites. For an anode-supported PEN structure, the concentration overpotential is usually very small at the cathode but can be significant at the anode, particularly at high current densities and fuel utilisation [48].

For open-circuit conditions, the reactant and product concentrations at the electrode/electrolyte interfaces or three-phase boundaries (TPB) are the same as those in the bulk channel flow, for which conditions the Nernst Eq. (22) gives the open-circuit potential. However, when the current is flowing and concentration gradients develop (as illustrated in Fig. 2 for an anode-supported SOFC), the species concentrations at the three-phase boundaries are different from the bulk concentrations. In such a case, the corresponding Nernst
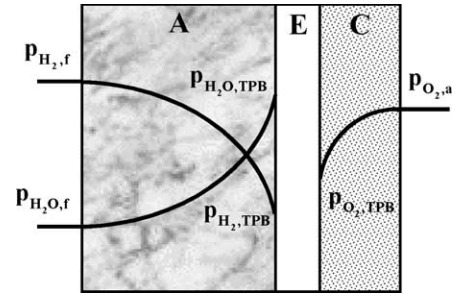

Fig. 2. Schematic diagram of an anode-supported solid oxide fuel cell.

equation is written as:

$$U_{\text{TPB}}^{\text{OCP}} = U_{\text{H}_2}^0 - \frac{\Re T}{2F} \ln\left(\frac{p_{\text{H}_2\text{O,TPB}}}{p_{\text{H}_2,\text{TPB}} p_{\text{O}_2,\text{TPB}}^{1/2}}\right). \tag{26}$$

The difference between Eqs. (22) and (26) gives the departure from the theoretical voltage,

$$\eta_{\text{conc}} = \frac{\Re T}{2F} \ln\left(\frac{p_{\text{H}_2\text{O,TPB}} p_{\text{H}_2,\text{f}}}{p_{\text{H}_2\text{O,f}} p_{\text{H}_2,\text{TPB}}}\right) + \frac{\Re T}{4F} \ln\left(\frac{p_{\text{O}_2,\text{a}}}{p_{\text{O}_2,\text{TPB}}}\right), \tag{27}$$

where the first term on the right-hand side refers to the anodic concentration overpotential, $\eta_{\text{conc,anode}}$.

$$\eta_{\text{conc,anode}} = \frac{\Re T}{2F} \ln\left(\frac{p_{\text{H}_2\text{O,TPB}} p_{\text{H}_2,\text{f}}}{p_{\text{H}_2\text{O,f}} p_{\text{H}_2,\text{TPB}}}\right), \tag{28}$$

and the second term to the cathodic concentration overpotential, $\eta_{\text{conc,cathode}}$,

$$\eta_{\text{conc,cathode}} = \frac{\Re T}{4F} \ln\left(\frac{p_{\text{O}_2,\text{a}}}{p_{\text{O}_2,\text{TPB}}}\right). \tag{29}$$

To allow for the calculation of η_{conc}, a relation between the partial pressures of H_2, H_2O, and O_2 at the three-phase boundaries and the current density is necessary. Different porous-media gas-phase transport models have been developed to predict concentration overpotentials [5,6,48,49]. Here, it has been assumed that: the principal gaseous species in the anode are H_2 and H_2O (equimolar counter-current one-dimensional diffusion of H_2 and H_2O) and in the cathode are O_2 and N_2 (one-dimensional self-diffusion); external diffusion is negligible; and the electrochemical reaction occurs only at the electrode/electrolyte interface [5,6,49]. The following equations were obtained:

$$p_{\text{H}_2,\text{TPB}} = p_{\text{H}_2,\text{f}} - \frac{\Re T \tau_{\text{anode}}}{2F D_{\text{eff,anode}}} j, \tag{30}$$

$$p_{\text{H}_2\text{O,TPB}} = p_{\text{H}_2\text{O,f}} + \frac{\Re T \tau_{\text{anode}}}{2F D_{\text{eff,anode}}} j, \tag{31}$$

$$p_{\text{O}_2,\text{TPB}} = P - (P - p_{\text{O}_2,\text{a}}) \exp\left(\frac{\Re T \tau_{\text{cathode}}}{4F D_{\text{eff,cathode}} P} j\right), \tag{32}$$

where τ_{anode} ($\tau_{cathode}$) denotes the thickness of the anode (cathode), $\overline{D_{eff,anode}}$ represents the average effective diffusivity coefficient in the anode (considering a binary gas mixture of H_2 and H_2O), and $D_{eff,cathode}$ represents the oxygen effective diffusivity coefficient in the cathode (binary gas mixture of O_2 and N_2). D_{eff} is related to the molecular diffusivity, $D_{molecular}$, by:

$$D_{eff,i} = \frac{\varepsilon_p}{\tau_{tortuosity}} D_{molecular,i}, \quad i \in \{H_2, H_2O, O_2, N_2\}. \tag{33}$$

This relation accounts for the complex pore structure inside the electrode material, where the diffusion path length along the pores is greater than the measurable electrode thickness. This is due to the pores' tortuous nature and pore constrictions, and thus the molecular diffusivity is corrected by a tortuosity factor, $\tau_{tortuosity}$, and the material porosity, ε_p. The tortuosity factor accounts for both the effects of altered diffusion path length and changing cross-sectional area in constrictions. The molecular diffusivity is the result of fluid–fluid intermolecular collisions as considered by the kinetic theory of gases, and is often known as the bulk diffusivity, D_{bulk}. When the pore size gets so small that it is less than the mean path of the fluid, fluid-wall collisions become the dominant ones and the mode of diffusive transport is altered to Knudsen diffusivity, $D_{knudsen}$, which arises from the kinetic theory of gases [50]. When both these types of diffusion, bulk and Knudsen, are important, both contribute to the molecular diffusivity, which is then given by:

$$\frac{1}{D_{molecular,i}} = \frac{1}{D_{bulk,i}} + \frac{1}{D_{knudsen,i}},$$
$$i \in \{H_2, H_2O, O_2, N_2\}. \tag{34}$$

2.3.3. Activation overpotentials

Activation overpotentials reflect the kinetics of reactions taking place on the electrode surface. At high operating temperatures, the electrode reaction is rapid and, as a result, the activation overpotential is usually small. However, as the operating temperature falls, activation overpotentials can become the most significant cause of voltage drop. Activation overpotentials are often represented by the non-linear Butler–Volmer equation, which relates the current density drawn to the activation overpotential and, for a first order charge transfer controlled electrochemical reaction, is given by:

$$j = j_{0,electrode} \left[\exp\left(\frac{\alpha n F}{\Re T} \eta_{act,electrode}\right) \right.$$
$$\left. - \exp\left(-\frac{(1-\alpha)n F}{\Re T} \eta_{act,electrode}\right) \right],$$
$$\text{electrode} \in \{\text{anode, cathode}\} \tag{35}$$

where α is the transfer coefficient (usually taken to be 0.5), n the number of electrons transferred in the single elementary

Table 5
Activation overpotential data for Eqs. (35)–(37)

$k_{cathode}$	$2.35 \times 10^{11}\ \Omega^{-1}\ m^{-2}$	$E_{cathode}$	$137\ kJ\ mol^{-1}$
k_{anode}	$6.54 \times 10^{11}\ \Omega^{-1}\ m^{-2}$	E_{anode}	$140\ kJ\ mol^{-1}$

rate-limiting reaction step represented by the Butler–Volmer equation, and $j_{0,electrode}$ the exchange current density, normally expressed as:

$$j_{0,electrode} = \frac{\Re T}{n F} k_{electrode} \exp\left(-\frac{E_{electrode}}{\Re T}\right),$$
$$\text{electrode} \in \{\text{anode, cathode}\}. \tag{36}$$

However, in the situation where charge transfer and mass transfer phenomena occur at comparable rates, the above Butler–Volmer equation needs to be corrected. The extended Butler–Volmer equation for the activation overpotential at the anode (the cathode concentration overpotential is subsequently shown to be negligible and, thus, does not require such an extended approach) is then given by:

$$j = j_{0,anode} \left[\frac{p_{H_2,TPB}}{p_{H_2,f}} \exp\left(\frac{\alpha n F}{\Re T} \eta_{act,anode}\right) \right.$$
$$\left. - \frac{p_{H_2O,TPB}}{p_{H_2O,f}} \exp\left(-\frac{(1-\alpha)n F}{\Re T} \eta_{act,anode}\right) \right]. \tag{37}$$

For a full knowledge of the activation overpotentials in a fuel cell, it is necessary to determine both the exchange current density and the transfer coefficient for both the anode and the cathode electrode reactions. As previously mentioned, much research is ongoing to improve electrode performance. However, although there are a large number of publications dealing with activation losses in IT-SOFCs, a full electrode analysis that can provide all the above data in a proven successful electrode is still difficult to obtain, as it requires both a detailed understanding of the electrode reaction mechanism and its microstructure. Here, for the cathode activation overpotential, the data provided by Horita et al. [51] is used. This data was obtained by studying the cathode reaction mechanism at the porous $La_{1-x}Sr_xCoO_{3-d}$ (LSC)/$La_{0.8}Sr_{0.2}Ga_{0.8}Mg_{0.2}O_{3-y}$ (LSGM) interface ($x = 0.2, 0.3, 0.4$) in the temperature range of 873–1073 K. This represents one of the few available comprehensive data sets, and simulations showed the data to be representative of more conventional YSZ-based materials. The parameters n and α in Eqs. (35)–(37) were set equal to 2 and 0.5, respectively (assuming a two-electron transfer rate-determining step). After fitting the available data ($x = 0.2$), the parameters presented in Table 5 were obtained. These lead to a cathode area specific resistance of $0.2\ \Omega\ cm^2$ at 1073 K, considered reasonable for IT-SOFC operation. For the anode, and given that no appropriate data was found, it was decided to use, as a first estimate, the data presented in Table 5. The selection of these data is based on the fact that most authors indicate anode activation enthalpies in the range 120–160 kJ mol^{-1} [52,53] and in the knowledge that an appropriate area specific resistance for

Table 6
Model performance factors

Fuel utilisation factor

$$U_{fuel} = \frac{\bar{j}LW}{(8Fy_{CH_4}^0 + 2Fy_{H_2}^0 + 2Fy_{CO}^0)F_{fuel}^0} \qquad (38)$$

Air ratio

$$\lambda_{air} = \frac{y_{O_2}^0 F_{air}^0}{\bar{j}LW/4F} \qquad (39)$$

Power density

$$P_{SOFC} = \bar{j}U \qquad (40)$$

Fuel efficiency

$$\varepsilon_{SOFC} = \frac{\bar{j}ULW}{(y_{CH_4}^0 LHV_{CH_4}^0 + y_{H_2}^0 LHV_{H_2}^0 + y_{CO}^0 LHV_{CO}^0)F_{fuel}^0} \qquad (41)$$

IT-SOFC anode materials should not be more than $0.1\ \Omega\ cm^2$ at 1073 K.

2.3.4. Performance factors

The resulting system of partial differential and algebraic Eqs. (1)–(6), (10)–(25), (28)–(34), (35) for electrode = cathode, and (36)–(37) is solved using *gPROMS ModelBuilder* 2.2.5 [54], with the finite difference method. The initial conditions for the dynamic model (which is used only on a subsequent publication to analyse the effect of load changes) are the initial steady-state solution to which a disturbance is then imposed. For the solution of the steady-state model, in addition to all geometry and property data and inlet temperatures and compositions, there are three degrees of freedom available for the complete solution of the system. One option usually adopted in the fuel cell field is to specify the average current density (or total current), the fuel utilisation factor, and the air ratio. These are given quantities from which the molar fluxes of fuel and air are then determined. The fuel utilisation factor is the fraction of the total inlet fuel that is used to produce electricity in the cell. The air ratio reflects the excess air, in relation to that which is stoichiometrically needed, that is supplied to the cell for cooling. Output parameters usually adopted are the power density and the fuel efficiency. The fuel efficiency represents the fraction of the total chemical energy in the inlet fuel that is converted into electrical energy (power). The net chemical energy consumed in a fuel cell is converted either to electrical energy or to heat generation due to entropy change of the electrochemical reactions, losses by overpotential effects, and resistance to current flow. Table 6 presents the mathematical definition of these performance factors.

3. Simulation results and discussion

This section is divided in four sub-sections: Section 3.1 introduces the model input parameters and inlet operating conditions; Section 3.2 presents the simulated curves for cell voltage and power density as a function of current density; Section 3.3 analyses the steady-state performance of a co-flow SOFC system; and Section 3.4 briefly compares the system steady-state performance under co and counter-flow operation.

3.1. Input parameters and inlet operating conditions

Table 7 presents the model input parameters: geometry and property data (properties of the materials and cell dimensions), inlet temperatures and gas compositions, average current density (or total current), fuel utilisation factor, and air ratio. All the physical property values of the cell materials are based on mean values from the literature [1,20,22,24,25,42,45]. The temperature dependence of the anode and cathode electronic conductivity is considered negligible in the temperature range of concern [42]. The PEN and interconnect emissivity values are considered typical of ceramic [42] and stainless steel materials, respectively. The cell dimensions are typical values for anode-supported intermediate-temperature SOFCs. The inlet fuel is considered as a gas mixture of CH_4, H_2O, CO, H_2, and CO_2. Its composition results from a mixture with a steam to carbon ratio equal to 2 after 10% pre-reforming, where the shift reaction is at equilibrium. The average current density value is chosen based on the curves presented in Section 3.2 and on the fact that fuel cells are normally designed to operate at a cell voltage between 0.6 and 0.7 V. This range of operation is found to be a good compromise between cell efficiency, power density, low capital cost, stable operation, and avoids possible anode oxidation at low cell voltage [5]. The air ratio value guarantees a temperature increase along the cell of around 100 K. The remaining model physical properties (gas stream densities, heat capacities, and thermal conductivities) and gas velocities are determined for the inlet conditions, assuming ideal gas behaviour [42,55], and are taken as constant values that apply throughout the system. The thermodynamic properties (reaction enthalpies and Gibbs free energy) are calculated as a function of temperature, assuming an ideal gas, by integration (according to the specific method rules) of the heat capacity of each component in the corresponding gas mixture [55]. The effective diffusivity coefficients are calculated assuming electrodes with 30% porosity ($\varepsilon_p = 0.30$), a tortuosity of $\tau_{tortuosity} = 6$, and an average pore radius (used to calculate the Knudsen diffusivity) of $0.5\ \mu m$ [5].

3.2. Cell voltage and power density as a function of current density

This section presents the characteristic curves for cell voltage and power density as a function of current density. Note

Table 7
Model input data and operating conditions

Physical properties of the cell materials			
Anode electrical conductivity, σ_{anode}	$80 \times 10^3\ \Omega^{-1}\ m^{-1}$	Cathode electrical conductivity, $\sigma_{cathode}$	$8.4 \times 10^3\ \Omega^{-1}\ m^{-1}$
PEN density, ρ_{PEN}	$5900\ kg\ m^{-3}$	Interconnect density, ρ_I	$8000\ kg\ m^{-3}$
PEN thermal conductivity, λ_{PEN}	$2 \times 10^{-3}\ kJ\ m^{-1}\ s^{-1}\ K^{-1}$	Interconnect thermal conductivity, λ_I	$25 \times 10^{-3}\ kJ\ m^{-1}\ s^{-1}\ K^{-1}$
PEN heat capacity, $C_{p,PEN}$	$0.5\ kJ\ kg^{-1}\ K^{-1}$	Interconnect heat capacity, $C_{p,I}$	$0.5\ kJ\ kg^{-1}\ K^{-1}$
Electrolyte ionic conductivity, $\sigma_{electrolyte}$	$33.4 \times 10^3\ exp(-10.3 \times 10^3/T)\ \Omega^{-1}\ m^{-1}$		
PEN emissivity, $\in_{PEN}$	0.8	Interconnect emissivity, $\in_I$	0.1
Anode diffusion coefficient, $D_{eff,anode}$	$3.66 \times 10^{-5}\ m^2\ s^{-1}$	Cathode diffusion coefficient, $D_{eff,cathode}$	$1.37 \times 10^{-5}\ m^2\ s^{-1}$
Dimensions of the cell elements			
Cell length, L	0.4 m	Anode thickness, τ_{anode}	500 μm
Cell width, W	0.1 m	Cathode thickness, $\tau_{cathode}$	50 μm
Fuel channel height, h_f	1 mm	Electrolyte thickness, $\tau_{electrolyte}$	20 μm
Air channel height, h_a	1 mm	Interconnect thickness, τ_I	500 μm
Operating conditions			
Fuel utilisation, U_{fuel}	75%	Pressure, P	1 bar
Average current density, $\bar{j}$	0.5 A cm^{-2}	Fuel inlet temperature, T_f^0	1023 K
Air ratio, λ_{air}	8.5	Air inlet temperature, T_a^0	1023 K
Air feed	21% O_2, 79% N_2	Fuel feed	Steam/carbon = 2, 10% pre-reforming

that such curves do not result from the solution of the full SOFC model in Section 2, but only from the electrochemical model in Section 2.3. The fuel composition in Figs. 3–5 is based on a fully reformed steam and methane mixture (with an initial steam to carbon ratio of 2), to which a degree of fuel utilisation (hydrogen and carbon monoxide) is then further applied.

Fig. 3 illustrates the predicted cell voltage and power density as a function of current density at 1073 K for an undepleted fully reformed fuel mixture; the individual contributions of all the various potential losses are also shown. As can be seen, the power density reaches a peak value

of 0.860 W cm^{-2} when the current density is 2.07 A cm^{-2} and the cell voltage 0.415 V. Under these conditions, the cathode activation and ohmic overpotentials represent the major losses within the cell, followed by the anode activation overpotential. Although the system under study is an anode-supported one, anode concentration overpotentials are relatively small, but still much higher than those at the cathode. A typical voltage versus current density curve normally presents a convex curvature caused by activation overpotentials for low current densities and a concave curvature associated with concentration losses for high current densities. When there is no fuel or oxidant at the three-phase boundary
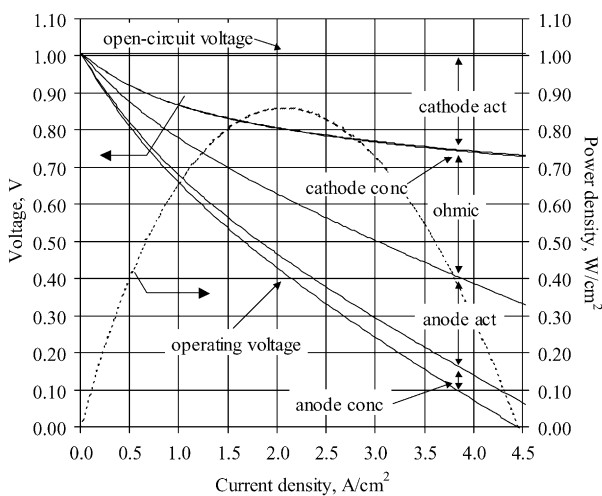

Fig. 3. Cell voltage and power density as a function of current density at 1073 K for an undepleted fully reformed fuel mixture. The solid lines are voltage curves (left axis) and the dashed line is the power density curve (right axis).
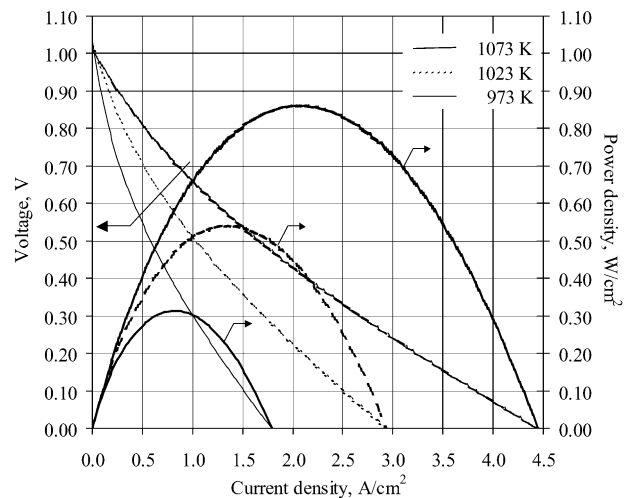

Fig. 4. Cell voltage and power density as a function of current density at 973, 1023, and 1073 K for an undepleted fully reformed fuel mixture. The thinner lines are voltage curves (left axis) and the thicker lines are power density curves (right axis).
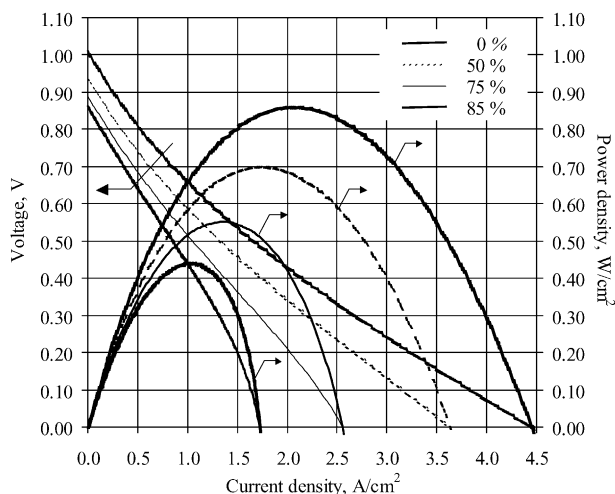
Fig. 5. Cell voltage and power density as a function of current density at 1073 K for a fully reformed fuel mixture with 0, 50, 75, and 85% fuel utilisation. The thinner lines are voltage curves (left axis) and the thicker lines are power density curves (right axis).

at the electrode/electrolyte interface, the concentration overpotentials become so large that the voltage reaches zero and the cell cannot operate. The current density at which this phenomenon occurs is often referred to as the limiting current density (anode or cathode limiting current density). However, whether or not a concave curvature is observed at high current densities depends on the particular cell operating conditions, design, and materials, which determine the relative magnitude of the ohmic and activation losses. For the cell and operating conditions illustrated in Fig. 3, no concave curvature is observed. This is mainly due to high ohmic and activation losses that cause the cell voltage to drop to zero when the current density reaches $4.45\,\mathrm{A\,cm^{-2}}$ (while the anode limiting current density of $10.1\,\mathrm{A\,cm^{-2}}$ is never reached). As mentioned previously, fuel cells are normally designed to operate at a cell voltage between 0.6 and 0.7 V. Thus, if the cell under study were to be operated at a constant temperature and gas composition, the best operating point, based on Fig. 3, would be between current density values of 0.823 and $1.23\,\mathrm{A\,cm^{-2}}$, which lead to power densities between 0.583 and $0.739\,\mathrm{W\,cm^{-2}}$.

All the above is valid for operation at 1073 K. However, and as pointed out before, one of the main incentives in using anode-supported SOFC designs is to allow a reduction in the operating temperature and, thus, the use of both metal and ceramic materials as compared to all-ceramic SOFCs. Thus, it is important to evaluate the cell performance at lower temperatures. Fig. 4 illustrates the predicted cell voltage and power density as a function of current density at 973, 1023, and 1073 K, for the same fuel composition as in Fig. 3. As expected, the performance of a cell is significantly hindered when the operating temperature is decreased: the maximum power density reduces from $0.860\,\mathrm{W\,cm^{-2}}$ at 1073 K, to $0.539\,\mathrm{W\,cm^{-2}}$ at 1023 K (at a current density of $1.36\,\mathrm{A\,cm^{-2}}$ and a voltage of 0.397 V) and to $0.314\,\mathrm{W\,cm^{-2}}$ at 973 K (at

a current density of $0.823\,\mathrm{A\,cm^{-2}}$ and a voltage of 0.381 V); and the point at which the cell voltage drops to zero reduces from $4.45\,\mathrm{A\,cm^{-2}}$ at 1073 K to $2.93\,\mathrm{A\,cm^{-2}}$ at 1023 K and to $1.79\,\mathrm{A\,cm^{-2}}$ at 973 K. The best operating point, applying the same criteria as above, now falls between current density values of 0.518 and $0.734\,\mathrm{A\,cm^{-2}}$ for 1023 K (which leads to power densities between 0.360 and $0.443\,\mathrm{W\,cm^{-2}}$) and between 0.269 and $0.428\,\mathrm{A\,cm^{-2}}$ for 973 K (which leads to power densities between 0.190 and $0.253\,\mathrm{W\,cm^{-2}}$).

Fuel composition plays a significant role in fuel cell performance. In operation and as the fuel flows through a SOFC fuel channel, hydrogen and carbon monoxide are consumed by the electrochemical reactions and the fuel stream becomes diluted, being less rich close to the exit of the channel. Therefore, in this region, concentration overpotentials become more significant. Fig. 5 illustrates the predicted cell voltage and power density as a function of current density for a fully reformed fuel mixture with 0, 50, 75, and 85% fuel utilisation. For 0 and 50% fuel utilisation, concentration overpotentials are not significant. As seen in Fig. 5, for these two cases, the voltage versus current density curve does not present a concave curvature for high current densities. However, for 75 and 85% fuel utilisation, the concavity becomes visible and voltage and power density drop more rapidly to zero, due to concentration overpotentials in the anode (cathode concentration overpotentials remain negligible). The anode limiting current density decreases significantly from $5.64\,\mathrm{A\,cm^{-2}}$ at 50% fuel utilisation, to $2.98\,\mathrm{A\,cm^{-2}}$ at 75% and $1.83\,\mathrm{A\,cm^{-2}}$ at 85%. However, as the activation overpotentials also take into account the effect of mass transport through Eq. (37), the point at which the cell voltage drops to zero occurs before (at $3.59\,\mathrm{A\,cm^{-2}}$ for 50% fuel utilisation, $2.55\,\mathrm{A\,cm^{-2}}$ for 75% and $1.71\,\mathrm{A\,cm^{-2}}$ for 85%).

In terms of reported values within the available literature, main results are: peak power densities of $1.08\,\mathrm{W\,cm^{-2}}$ at 973 K and $1.58\,\mathrm{W\,cm^{-2}}$ at 1073 K [49] or $0.49\,\mathrm{W\,cm^{-2}}$ at 1073 K [5] for anode-supported SOFCs operating on humidified hydrogen, and $0.40\,\mathrm{W\,cm^{-2}}$ at 1023 K for an anode-supported SOFC operating on methane [48]. Important to note is the fact that, although very high power densities have been reported for single cell test by SOFC developers, no data is yet available to allow for the validation of developed models. In addition, it should also be noted that power density values for stack operation are, as confirmed in Section 3.3, well below single cell values.

3.3. Anode-supported IT DIR-SOFC operation

The model described in Section 2 is able to predict the various temperatures along the cell length (fuel and air channels, PEN structure, and interconnect), the gas composition in the fuel and air channels, all the electrochemical-related variables (open-circuit voltage, activation, ohmic, and concentration overpotential losses, terminal potential, and current density) as well as the cell efficiency and power output. Figs. 6–8
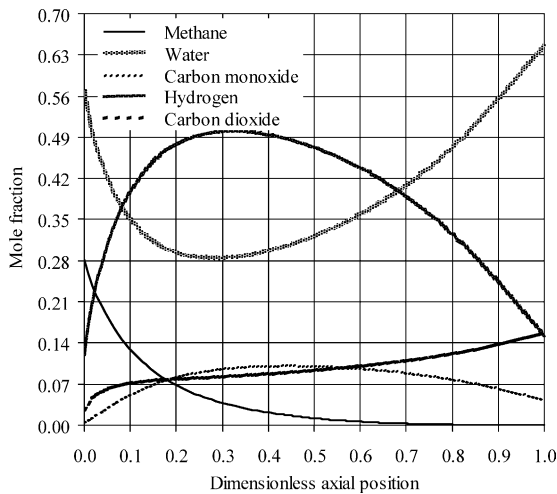
Fig. 6. Fuel channel component mole fractions along the cell length for the conditions in Table 7.

Fig. 8. Predicted voltage, current density, and contribution of all the various potential losses along the cell length for the conditions in Table 7.

present some of these variables for the operating conditions given in Table 7. Figs. 6–8 are for a co-flow operation case, while Figs. 12–14, in Section 3.4, are for counter-flow operation.

Fig. 6 presents the mole fraction profiles along the cell length of all the components in the fuel channel stream. These illustrate the impact of the simultaneous occurrence of the direct internal reforming reaction, the water gas-shift reaction, and the oxidation of hydrogen at the anode/electrolyte interface. At the entrance of the fuel cell, and due to the high methane content, the reforming reaction is much faster and the methane starts being consumed rapidly, producing hydrogen and carbon monoxide. Once most of the methane is consumed, the hydrogen oxidation reaction becomes the faster reaction and the consumption of hydrogen and production of steam can be clearly seen. The current density profile along the cell length, shown in Fig. 8, corroborates the increasing
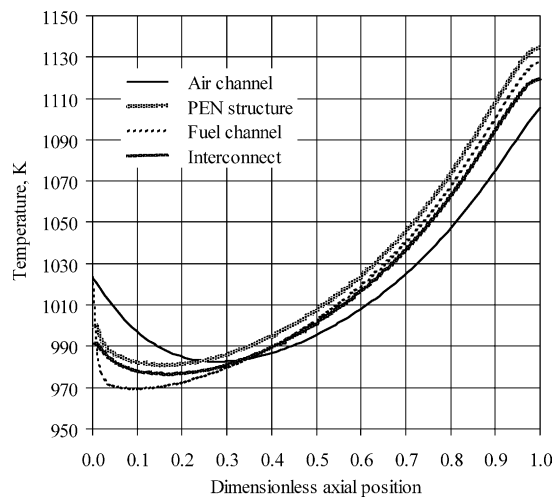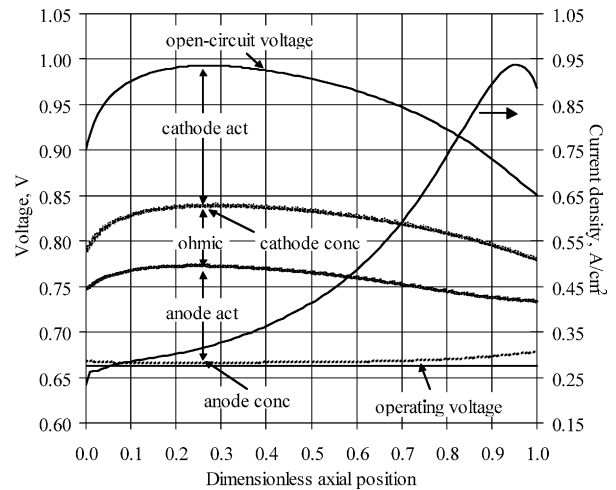

Fig. 7. Fuel and air channels, PEN structure, and interconnect temperature along the cell length for the conditions in Table 7.

hydrogen oxidation reaction along the cell. At the exit of the fuel channel, all the methane has been fully consumed and the stream content is 65% in H_2O, 4% in CO, 15% in H_2, and 16% in CO_2.

Fig. 7 presents the fuel and air channels, PEN structure, and interconnect temperature profiles along the cell length. It can be seen that the cell temperature increases along the fuel and air flow directions by heat accumulation, with the maximum temperature occurring at the outlet. This temperature distribution is typical of a co-flow arrangement. Although, the steam reforming reaction is known to be strongly endothermic, it can be seen that there is enough heat production in the cell to enable the reaction. The total heat consumed by the DIR reaction represents 45% of the total heat produced in the cell. The simulations do illustrate a slight local cooling effect associated with the reforming of methane, where the fuel channel temperature decreases by 54 K in relation to its inlet value (the equivalent temperature decrease in the PEN structure is only 18 K). As mentioned before, direct or indirect internal reforming in typical high-temperature SOFCs, where the inlet temperature is normally 1173 K, is characterised by severe local cooling effects at the cell entrance. The profiles in Fig. 7 then demonstrate that intermediate-temperature SOFCs can represent a great improvement in this area. Also, note that the extent of pre-reforming assumed for these simulations is of only 10%, and thus the inlet fuel is very rich in methane. The maximum and minimum temperatures in the PEN structure are 1135 and 981 K, respectively, leading to a maximum temperature difference of 154 K in the cell. Temperature gradients in a solid oxide fuel cell stack (along the length and across the various layers) need to be carefully monitored to avoid any thermally induced fractures on its ceramic components, with a consequent cell failure.

Finally, Fig. 8 shows the predicted voltage and current density along the cell length, as well as the individual contribution of all the various potential losses. As discussed before, for a given cell, the potential losses and current density
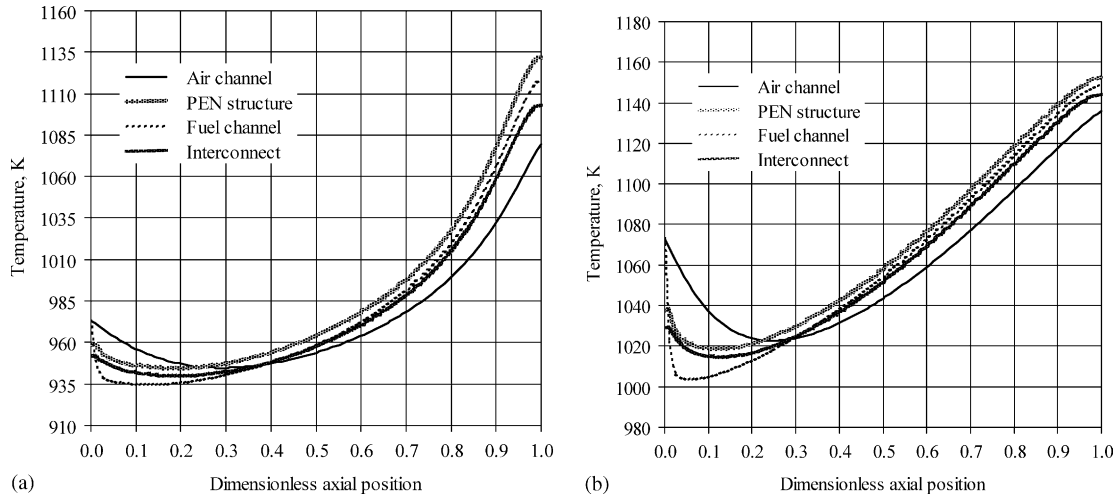
Fig. 9. Fuel and air channels, PEN structure, and interconnect temperature along the cell length for the conditions in Table 7, except that the fuel and air inlet temperatures are: (a) 973 K and (b) 1073 K.

distribution along the cell are related to the composition of the gas streams and to the various temperatures in the cell. The open-circuit potential is governed by the Nernst equation, and thus follows both the cell temperature and the partial pressure of hydrogen, as this is produced by DIR and then oxidised and replaced by steam. As the temperature increases along the cell length, the overpotentials decrease, allowing for an increase of the current density. The concentration overpotentials, even though very small in the case under study, increase as the fuel is consumed along the cell. In percentage terms, the cathode activation overpotentials represent 45% of the total losses within the cell, followed by the anode activation overpotentials with 31%, and the PEN structure ohmic losses with 22%. The anode concentration overpotentials contribute to 2% of the losses while the losses by cathode concentration overpotentials were found negligible (expected, given the reduced cathode thickness and oxygen utilisation). This is the expected trend for an IT-SOFC, where the electrolyte is thin and ohmic losses no longer dominate. For the op-

erating conditions in Table 7, the SOFC under study has a satisfactory terminal voltage of 0.663 V, a power density of 0.332 W cm^{-2}, and a fuel efficiency of 46.8%.

Figs. 9–11 illustrate the effect of changing some of the operating conditions. Fig. 9 presents the fuel and air channels, PEN structure, and interconnect temperature profiles along the cell length for the cases where the fuel and air inlet temperatures are 973 and 1073 K (all the remaining conditions in Table 7 are kept constant). From Figs. 7 and 9, it can be seen that as the inlet temperature increases, the temperature gradients at the entrance of the fuel channel also increase. This is due to an increase in the steam reforming reaction rate with higher temperatures. However, the overall temperature increase across the cell length decreases. This is because, at a given current density, higher temperatures lead to a more electrically efficient operation (the fuel cell efficiency is 40.2% for fuel and air inlet temperatures of 973 K and 52.0% for 1073 K), and thus to a lower heat generation in the cell. This implies that if the studied SOFC needs to
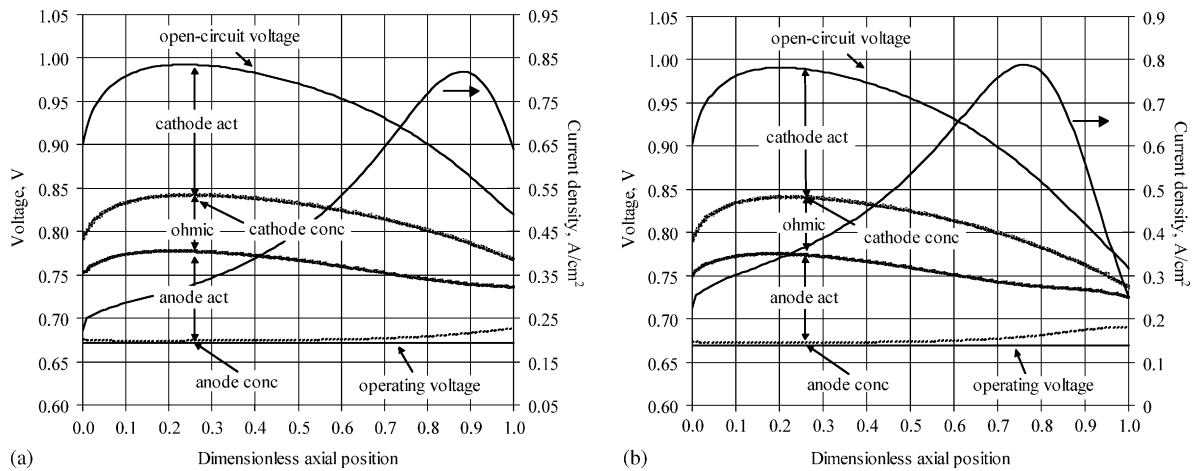

Fig. 10. Predicted voltage, current density, and contribution of all the various potential losses along the cell length for the conditions in Table 7, except that the fuel utilisation is: (a) 85% and (b) 95%.
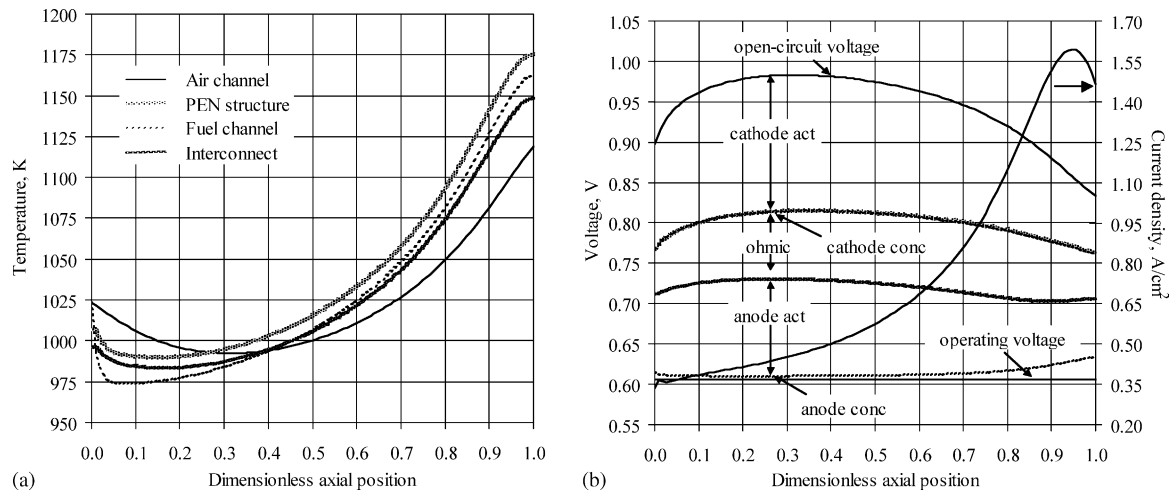
Fig. 11. Fuel and air channels, PEN structure, and interconnect temperature and predicted voltage, current density, and individual contribution of all the various potential losses along the cell length for the conditions in Table 7, except that the average current density is 0.75 A cm^{-2}.

be operated at lower temperatures while keeping the overall temperature gradient across the cell of 100 K, the air ratio needs to be increased.

Fig. 10 presents the predicted voltage, current density, and individual contributions of all the various potential losses along the cell length for the cases where the fuel utilisation is changed to 85 and 95%. The purpose of showing Fig. 10 is to illustrate the effect of concentration overpotentials on the cell performance. As can be seen, as the fuel is consumed along the cell, concentration overpotentials become more significant and the current density that can be locally drawn drops considerably to maintain a constant voltage. This effect is also accentuated because the open-circuit voltage decreases significantly with the consumption of hydrogen. As expected, the fuel efficiency increases with an increase in fuel utilisation (53.6% for a fuel utilisation of 85% and 59.8 for 95%). However, and since the amount of inlet fuel, and thus the amount of heat consumed to reform all the methane is much lower, the overall temperature profiles are similar to those presented in Fig. 7.

Fig. 11 presents the fuel and air channels, PEN structure, and interconnect temperature and predicted voltage, current density, and individual contribution of all the various potential losses along the cell length for the case where the cell is operated at an average current density of 0.75 A cm^{-2}. It can be seen that, with an increase in current density, the cell temperature increases. This implies that to maintain a constant total temperature increase along the cell, an increase in the air ratio is required. From Fig. 11b, it can be seen that an increase in current density leads to an increase in all the overpotential losses in a cell and thus to a lower operating voltage. At 0.75 A cm^{-2}, the cell voltage decreases to 0.606 V, the power density is 0.455 W cm^{-2}, and the fuel efficiency 42.7%. In summary, temperatures, fuel composition, gas flowrates, and current density, greatly affect the cell performance and source of operation losses. The best combination of operating conditions will always be a compromise of several factors, not

only related to the cell stack but to all the balance of plant involving it.

3.4. Anode-supported IT DIR-SOFC operation: co-flow versus counter-flow operation

This last section aims to present a brief comparison of the system behaviour under co and counter-flow operation. The air channel mass and energy balances and corresponding boundary conditions (Eqs. (4) and (5) in Table 1 and Eqs. (15) and (16) in Table 4) have been modified accordingly and the same operating conditions as the ones given in Table 7 have been considered.

Figs. 12–14 present the fuel and air channels, PEN structure, and interconnect temperature profiles, the mole fraction profiles of all the components in the fuel channel gas stream, and the voltage, current density, and individual contribution of all the various potential losses, along the cell length for
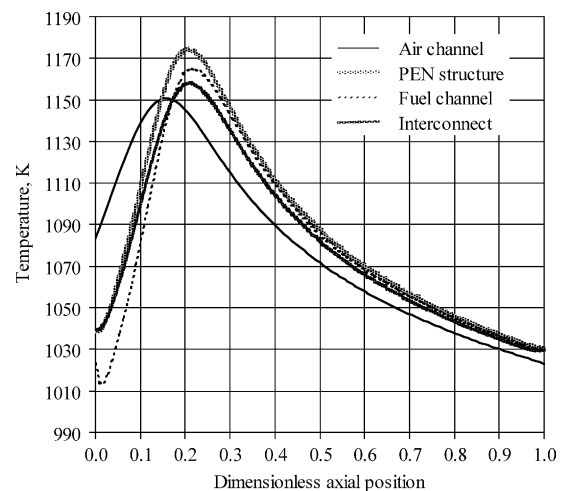

Fig. 12. Fuel and air channels, PEN structure, and interconnect temperature along the cell length for the conditions in Table 7 for counter-flow operation.
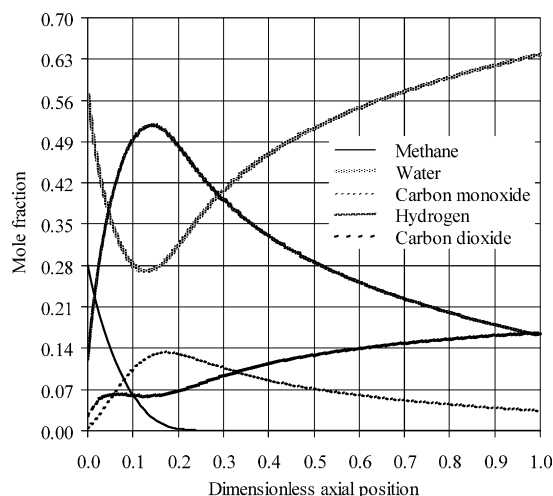
Fig. 13. Fuel channel component mole fractions along the cell length for the conditions in Table 7 for counter-flow operation.

counter-flow operation. Figs. 6–8 above present the equivalent co-flow operation figures.

Comparing Figs. 7 and 12 it can be seen that, while in a co-flow SOFC the temperature increases along the air and fuel flow direction by heat accumulation, with the maximum temperature at the exit, in a counter-flow cell the temperature profile has a peak near the air channel exit and the operation is characterised by higher average cell temperatures and steeper local temperature gradients. Comparing Figs. 6 and 13 it is observed that, under counter-flow operation, and since the temperature close to the fuel channel entrance is higher (Fig. 12), all the methane is fully reformed in the first 20% of the cell length, while in the co-flow case, methane is gradually reformed along the fuel channel length. As discussed above, temperature gradients in a SOFC stack need to be carefully monitored to avoid any thermally induced

fractures on its ceramic components. This seems to represent the major drawback of SOFC operation under counter-flow of the fuel and air gas streams: in the co-flow operation case the simulations illustrate only a slight local cooling effect associated with DIR (Fig. 7); but in the counter-flow case the temperature has a steep 135 K increase in the first 8 cm of the fuel channel. Fig. 14 illustrates once again how the various voltage losses and the current density distribution are related to gas composition and cell temperature: the open-circuit voltage follows both the cell temperature and partial pressures of hydrogen and steam; and the concentration over-potentials, even though negligible for the simulated operating conditions, are more pronounced for higher local current densities.

Finally, for the operating conditions in Table 7, this counter-flow SOFC system has a terminal voltage of 0.771 V, a power density of 0.386 W cm^{-2}, and a fuel efficiency of 54.4%. The considerably better performance observed for the SOFC system operating under counter-flow is an outcome of the higher average cell temperatures and consequent lower cell activation overpotentials and ohmic losses. However, because of the steep temperature gradients in Fig. 12, not desirable for a ceramic system, and the consequent uneven current density distribution (Fig. 14), counter-flow is not considered the best mode of operation. Achenbach [29] reached similar conclusions for a high-temperature SOFC system.

4. Conclusions

A dynamic anode-supported intermediate-temperature direct internal reforming planar one-dimensional SOFC stack model has been presented. The model developed consists of mass and energy balances, and an electrochemical model that relates the fuel and air gas composition and temperature to voltage, current density, and other relevant fuel cell variables. The electrochemical performance of the cell has been analysed for several temperatures and fuel utilisations. Maximum power densities of 0.86 W cm^{-2} for a current density of 2.1 A cm^{-2} and a cell voltage 0.42 V have been reported for an undepleted fully reformed fuel mixture at 1073 K. The steady-state performance of the cell as well as the impact of changes in inlet temperatures, fuel utilisation, average current density, and flow configuration have been illustrated. The SOFC system studied operates at an output voltage of 0.66 V, a power density of 0.33 W cm^{-2}, and a fuel efficiency of 47%, when using a 10% pre-reformed methane fuel mixture with 75% fuel utilisation, inlet fuel and air temperatures of 1023 K, average current density of 0.5 A cm^{-2}, and an air ratio of 8.5. It has been shown that, for similar operating conditions, SOFC operation under counter-flow of the fuel and air gas streams leads to steep temperature gradients with a consequent uneven current density distribution, and hence, is not considered the best mode of operation. The model presented is used, in a subsequent publication, to analyse the dynamic
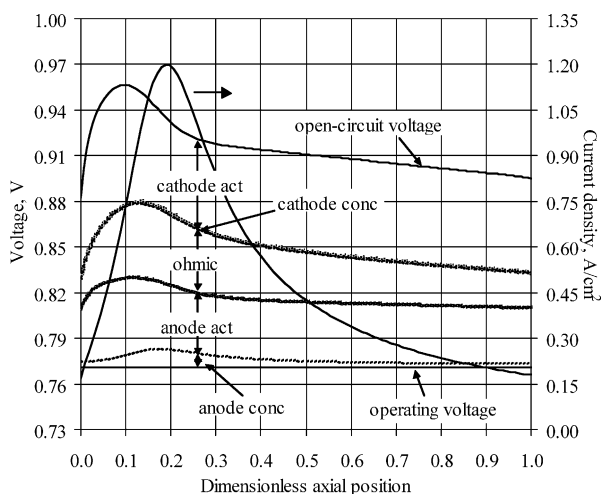

Fig. 14. Predicted voltage, current density, and contribution of all the various voltage losses along the cell length for the conditions in Table 7 for counter-flow operation.

response of the described anode-supported IT DIR-SOFC to possible load changes [19].

References

[1] J.R. Ferguson, J.M. Fiard, R. Herbin, Three-dimensional numerical simulation for various geometries of solid oxide fuel cells, J. Power Sour. 58 (1996) 109–122.

[2] O. Yamamoto, Solid oxide fuel cells: fundamental aspects and prospects, Electrochim. Acta 45 (2000) 2423–2435.

[3] S.P.S. Badwal, K. Foger, Solid oxide electrolyte fuel cell review, Ceramics Int. 22 (1996) 257–265.

[4] J.P.P. Huijsmans, Ceramics in solid oxide fuel cells, Curr. Opin. Solid State Mater. Sci. 5 (2001) 317–323.

[5] S.H. Chan, K.A. Khor, Z.T. Xia, A complete polarization model of a solid oxide fuel cell and its sensitivity to the change of cell component thickness, J. Power Sour. 93 (2001) 130–140.

[6] A.V. Virkar, J. Chen, C.W. Tanner, J. Kim, The role of electrode microstructure on activation and concentration polarizations in solid oxide fuel cells, Solid State Ionics 131 (2000) 189–198.

[7] A.L. Dicks, Advances in catalysts for internal reforming in high temperature fuel cells, J. Power Sour. 71 (1998) 111–122.

[8] A.L. Dicks, Hydrogen generation from natural gas for the fuel cell systems of tomorrow, J. Power Sour. 61 (1996) 113–124.

[9] S.H. Clarke, A.L. Dicks, K. Pointon, T.A. Smith, A. Swann, Catalytic aspects of the steam reforming of hydrocarbons in internal reforming fuel cells, Catal. Today 38 (1997) 411–423.

[10] J. Rostrup-Nielsen, L.J. Christiansen, Internal steam reforming in fuel cells and alkali poisoning, Appl. Catal. A: Gen. 126 (1995) 381–390.

[11] N. Nakagawa, H. Sagara, K. Kato, Catalytic activity of Ni–YSZ–CeO$_2$ anode for the steam reforming of methane in a direct internal-reforming solid oxide fuel cell, J. Power Sour. 92 (2001) 88–94.

[12] A.L. Lee, R.F. Zabransky, W.J. Huber, Internal reforming development for solid oxide fuel cells, Ind. Eng. Chem. Res. 29 (1990) 766–773.

[13] K. Ahmed, K. Foger, Kinetics of internal steam reforming of methane on Ni/YSZ-based anodes for solid oxide fuel cells, Catal. Today 63 (2000) 479–487.

[14] S. Park, R.J. Gorte, J.M. Vohs, Applications of heterogeneous catalysis in the direct oxidation of hydrocarbons in a solid-oxide fuel cell, Appl. Catal. A: Gen. 200 (2000) 55–61.

[15] P. Aguiar, D. Chadwick, L. Kershenbaum, Modelling of an indirect internal reforming solid oxide fuel cell, Chem. Eng. Sci. 57 (2002) 1665–1677.

[16] R. Fellows, A novel configuration for direct internal reforming stacks, J. Power Sour. 71 (1998) 281–287.

[17] J. Meusinger, E. Riensche, U. Stimming, Reforming of natural gas in solid oxide fuel cell systems, J. Power Sour. 71 (1998) 315–320.

[18] E. Achenbach, E. Riensche, Methane/steam reforming kinetics for solid oxide fuel cells, J. Power Sour. 52 (1994) 283–288.

[19] P. Aguiar, C.S. Adjiman, N.P. Brandon, Anode-supported intermediate-temperature direct internal reforming solid oxide fuel cell. II: Model-based dynamic performance and control. J. Power Sour., submitted for publication.

[20] K.P. Recknagle, R.E. Williford, L.A. Chick, D.R. Rector, M.A. Khaleel, Three-dimensional thermo-fluid electrochemical mo1deling of planar SOFC stacks, J. Power Sour. 113 (2003) 109–114.

[21] S. Nagata, A. Momma, T. Kato, Y. Kasuga, Numerical analysis of output characteristics of tubular SOFC with internal reformer, J. Power Sour. 101 (2001) 60–71.

[22] M. Iwata, T. Hikosaka, M. Morita, T. Iwanari, K. Ito, K. Onda, Y. Esaki, Y. Sakaki, S. Nagata, Performance analysis of planar-type unit SOFC considering current and temperature distributions, Solid State Ionics 132 (2000) 297–308.

[23] S.G. Neophytides, The reversed flow operation of a crossflow solid oxide fuel cell monolith, Chem. Eng. Sci. 54 (1999) 4603–4613.

[24] N.F. Bessette II, W.J. Wepfer, J. Winnick, A mathematical model of a solid oxide fuel cell, J. Electrochem. Soc. 142 (1995) 3792–3800.

[25] S. Ahmed, C. McPheeters, R. Kumar, Thermal-hydraulic model of a monolithic solid oxide fuel cell, J. Electrochem. Soc. 138 (1991) 2712–2718.

[26] T. Ota, M. Koyama, C. Wen, K. Yamada, H. Takahashi, Object-based modeling of SOFC system: dynamic behavior of micro-tube SOFC, J. Power Sour. 118 (2003) 430–439.

[27] D.J. Hall, R.G. Colclaser, Transient modeling and simulation of a tubular solid oxide fuel cell, IEEE Trans. Energ. Conv. 14 (1999) 749–753.

[28] E. Achenbach, Response of a solid oxide fuel cell to load change, J. Power Sour. 57 (1995) 105–109.

[29] E. Achenbach, Three-dimensional and time-dependent simulation of a planar solid oxide fuel cell stack, J. Power Sour. 49 (1994) 333–348.

[30] H. Park, Y. Lee, M. Kim, G. Chung, S. Nam, S. Hong, T. Lim, H. Lim, Studies of the effects of the reformer in an internal-reforming molten carbonate fuel cell by mathematical modeling, J. Power Sour. 104 (2002) 140–147.

[31] K. Ahmed, K. Foger, Approach to equilibrium of the water-gas shift reaction on a Ni/zirconia anode under solid oxide fuel-cell conditions, J. Power Sour. 103 (2001) 150–153.

[32] H. Yakabe, T. Ogiwarw, M. Hishinuma, I. Yasuda, 3-D model calculation for planar SOFC, J. Power Sour. 102 (2001) 144–154.

[33] X. Guo, K. Hidajat, C. Ching, Simulation of a solid oxide fuel cell for oxidative coupling of methane, Catal. Today 50 (1999) 109–116.

[34] M.V. Twigg, Catalyst Handbook, 2nd ed., Manson Publishing, 1996.

[35] J. Xu, G.F. Froment, Methane steam reforming, methanation and water-gas shift: I Intrinsic kinetics, AIChE J. 35 (1989) 88–96.

[36] J. Rostrup-Nielsen, Catalytic Steam Reforming. Catalysis: Science and Technology, Springer-Verlag, Berlin, 1984.

[37] V.D. Belyaev, T.I. Politova, O.A. Mar'ina, V.A. Sobyanin, Internal steam reforming of methane over Ni-based electrode in solid oxide fuel cells, Appl. Catal. A: Gen. 133 (1995) 47–57.

[38] A.L. Dicks, K.D. Pointon, A. Siddle, Intrinsic reaction kinetics of methane steam reforming on a nickel/zirconia anode, J. Power Sour. 86 (2000) 523–530.

[39] R. Peters, R. Dahl, U. Klüttgen, C. Palm, D. Stolten, Internal reforming of methane in solid oxide fuel cell systems, J. Power Sour. 106 (2002) 238–244.

[40] S. Bebelis, A. Zeritis, C. Tiropani, S.G. Neophytides, Intrinsic kinetics of the internal steam reforming of CH$_4$ over a Ni–YSZ-cermet catalyst-electrode, Ind. Eng. Chem. Res. 39 (2000) 4920–4927.

[41] J. Palsson, A. Selimovic, L. Sjunnesson, Combined solid oxide fuel cell and gas turbine systems for efficient power and heat generation, J. Power Sour. 86 (2000) 442–448.

[42] U.G. Bossel, Facts and Figures, Final Report on SOFC Data, IEA report. Swiss Federal Office of Energy, Operating task II, Berne, 1992.

[43] F.P. Incropera, D.P. De Witt, Fundamentals of Heat and Mass Transfer, 3rd ed., Wiley, Singapore, 1990.

[44] K. Kordesch, G. Simader, Fuel Cells and Their Applications, VCH, New York, 1996.

[45] N.Q. Minh, T. Takahashi, Science and Technology of Ceramic Fuel Cells, Elsevier, Amsterdam, 1995.

[46] C. Haynes, W.J. Wepfer, 'Design for power' of a commercial grade tubular solid oxide fuel cell, Energ. Conv. Manage. 41 (2000) 1123–1139.

[47] L. Petruzzi, S. Cocchi, F. Fineschi, A global thermo-electrochemical model for SOFC systems design and engineering, J. Power Sour. 118 (2003) 96–107.

[48] H. Zhu, R.J. Kee, A general mathematical model for analyzing the performance of fuel-cell membrane-electrode assemblies, J. Power Sour. 117 (2003) 61–74.

[49] J. Kim, A.V. Virkar, K. Fung, K. Mehta, S.C. Singhal, Polarization effects in intermediate temperature, anode-supported solid oxide fuel cells, J. Electrochem. Soc. 146 (1999) 69–78.

[50] G.F. Froment, K.B. Bischoff, Chemical Reactor Analysis and Design, 2nd ed., Wiley, 1990.

[51] T. Horita, K. Yamaji, N. Sakai, H. Yokokawa, A. Weber, E. Ivers-Tiffee, Electrode reaction of $La_{1-x}Sr_xCoO_{3-\delta}$ cathodes on $La_{0.8}Sr_{0.2}Ga_{0.8}Mg_{0.2}O3$-y electrolyte in solid oxide fuel cells, J. Electrochem.Soc. 148 (2001) A456–A462.

[52] S.P. Jiang, S.P.S. Badwal, An electrode kinetics study of H_2 oxidation on Ni/Y_2O_3-ZrO_2 cermet electrode of the solid oxide fuel cell, Solid State Ionics 123 (1999) 209–224.

[53] P. Holtappels, I.C. Vinke, L.G.J. de Haart, U. Stimming, Reaction of hydrogen/water mixtures on nickel-zirconia cermet electrodes II. AC polarization characteristics, J. Electrochem. Soc. (1999) 146.

[54] Process Systems Enterprise Ltd. gPROMS Introductory User Guide. London, 2002.

[55] R.C. Reid, J.M. Prausnitz, B.E. Poling, The Properties of Gases and Liquids, 4th ed., McGraw Hill, New York, 1988.